Research Article

Journal of Environmental Nanotechnology

Sustainable Mechanochemical Fabrication of $NiFe_2O_4$@rGO Conductive Hybrid for Energy Storage and Environmental Remediation

V. Y. Ganvir[1*], Syed Nadeem Ahmed Alvi[2], Pramod G. Musrif[3], M. Vadivel[4], P Satish Kumar[5] and Nestor Ulloa[6]

[1]Department of Applied Physics, Yeshwantrao Chavan College of Engineering, Nagpur, MH, India
[2]Department of Mechanical Engineering, J. D. College of Engineering, Nagpur, MH, India
[3]Department of Engineering Sciences, AISSMS, Institute of Information Technology, Shivajinagar, Pune, MH, India
[4]Department of Civil Engineering, Nehru Institute of Technology, Coimbatore, TN, India
[5]Department of Mechanical Engineering, Rathinam Technical campus, Coimbatore, TN, India
[6]Department of Mechanical Engineering, Escuela Superior Politécnica de Chimborazo (ESPOCH), Riobamba, Ecuador
Received: 23.12.2025 Accepted: 07.02.2026 Published: 30.03.2026
*vyganvir@gmail.com

ABSTRACT

This study reports a green, mechanochemical one-pot synthesis of a nickel ferrite/reduced graphene oxide ($NiFe_2O_4$@rGO) hybrid designed for dual applications in energy storage and environmental remediation. The integration of $NiFe_2O_4$ nanoparticles with rGO forms a conductive nano-network that significantly enhances charge transport and interfacial redox activity. In a three-electrode configuration using 4.0 M NaOH electrolyte, the $NiFe_2O_4$@rGO hybrid delivers a high specific capacitance of 496 F g^{-1} at a current density of 1 A g^{-1}, markedly outperforming pristine $NiFe_2O_4$. A symmetric supercapacitor assembled from the hybrid exhibits a specific capacitance of ~103 F g^{-1} at 1 A g^{-1} with an excellent cycling stability, retaining 93.16% of its initial capacitance after 5000 charge–discharge cycles. In addition, the $NiFe_2O_4$@rGO hybrid demonstrates outstanding photocatalytic activity, achieving over 99% degradation of rhodamine B dye within 60 min under UV irradiation, along with high reusability and structural stability. The enhanced electrochemical and photocatalytic performances are attributed to the synergistic interaction between $NiFe_2O_4$ and rGO, which promotes efficient electron transport and active site utilization. This work presents a scalable, eco-friendly synthesis strategy for a multifunctional hybrid material capable of bridging high-performance supercapacitor technology and wastewater treatment applications.

Keywords: Photocatalysts; Graphene oxide; Pseudocapacitive behavior; Rhodamine B dye; Ecofriendly.

1. INTRODUCTION

The two main concerns of sustainable energy systems are energy conservation and the reduction of environmental contamination (Anantha *et al.* 2025). A GO-supported ternary ferrite composite ($NiFe_2O_4$–$MnFe_2O_4$–$CoFe_2O_4$) delivered high energy density of 50.5 Wh kg^{-1} excellent cycling stability. The material demonstrated strong potential as anode for supercapacitors (Moradi and Ghobadi, 2024). Despite extensive studies on $NiFe_2O_4$–rGO hybrids, most rely on multistep, solvent-intensive synthesis and focus mainly on energy storage, leaving a gap in sustainable routes for dual-function materials. Mechanochemical synthesis offers an eco-friendly, scalable alternative to simultaneously achieve strong interfacial coupling and integrated supercapacitor–photocatalytic performance.

The cycling stability and superior performance (rGO/$NiFe_2O_4$/polyaniline) arose from synergistic EDLC and pseudocapacitive charge-storage mechanisms (Sardana *et al.* 2022). Binder-free $NiFe_2O_4$@Fe_3O_4@Fe_2N composites grown at N-doped rGO-wrapped nickel foam exhibited high pseudocapacitive behavior and whole-electrode capacitance. Flexible all-solid-state device achieved high power density (1670.4 W kg^{-1}) and energy density (92.8 Wh kg^{-1}) (Jiang *et al.* 2021). A hollow-cube hierarchical $NiFe_2O_4$–NiCo-LDH@rGO composite delivered a high SC of 750 C g^{-1} with excellent cycling durability, an energy density of 50 Wh kg^{-1} and also demonstrated promising electrochemical glucose sensing performance (Chu *et al.* 2020). Hydrothermally synthesized $NiFe_2O_4$ microstructures exhibited a pure cubic spinel phase and delivered a high SC of 744 F g^{-1} with 88% retention over 10,000 cycles and confirm $NiFe_2O_4$ microstructures as robust electrode materials for advanced supercapacitors (Hiragond *et al.* 2025).

The hybrid device $NiFe_2O_4$@PANI composites demonstrated good cycling stability with power and energy densities of 900 W kg^{-1} and 13.5 Wh kg^{-1}

(Alburaih *et al.* 2025). Bi-doped $NiFe_2O_4$ nanoparticles exhibited enhanced electrochemical and magnetic memory behavior, with the 20% Bi-doped sample achieving 339.16 F g^{-1} and 90.76% retention over 5000 cycles. Two-electrode results confirmed their suitability for practical supercapacitor devices (Hsu *et al.* 2025). Ag-$NiFe_2O_4$ nanoparticles uniformly dispersed on graphene nanoplatelets delivered a high SC of 913 F g^{-1} due to synergistic interfacial effects. (Saha *et al.* 2025). ZnO–$NiFe_2O_4$ nanocomposites exhibited tunable optical, dielectric, and magneto-capacitance properties with improved antimicrobial activity (Veeramani *et al.* 2025). $ZnFe_2O_4$/$NiFe_2O_4$/CeO_2 ternary nanocomposites showed enhanced surface area and electrochemical reversibility, achieving 102.4 F g^{-1} at 0.25 A g^{-1} (Manohar *et al.* 2024).

Tannic acid–based bio-epoxy was developed and used to fabricate hybrid *Ziziphus jujuba* seed particle / *Holoptelea integrifolia* fiber composites. Fuzzy logic model accurately predicted tensile, impact, and flexural strengths with an overall prediction accuracy of 87% (Kandavalli *et al.* 2025). The electrodes demonstrated good stability, indicating suitability for high-performance supercapacitor uses (Khawale *et al.* 2024). A hydrothermally synthesized $MgCr_2O_4$/rGO nanohybrid delivered a high SC of 1083.51 F g^{-1} with 96.08% retention after 4000 cycles. The reduced solution resistance and enhanced Faradaic kinetics confirmed its suitability for supercapacitor electrodes (Razzaq *et al.* 2026). A ternary $MnFe_2O_4$/rGO/SnS_2 nanocomposite synthesized hydrothermally achieved a high SC of 1068 F g^{-1} at 3 A g^{-1}. The electrode also delivered energy density of 38.86 Wh kg^{-1} with good power capability (Sahoo *et al.* 2026).

The novelty of this work lies in the green mechanochemical one-pot synthesis of $NiFe_2O_4$@rGO hybrid, which simultaneously integrates energy storage and photocatalytic functionalities within a single multifunctional material. Unlike conventional multistep or solvent-intensive synthesis routes, the proposed mechanochemical approach offers a simple, scalable, and eco-friendly strategy for constructing intimate interfacial coupling between nickel ferrite nanoparticles and reduced graphene oxide. The study uniquely demonstrates how rGO acts as a conductive nano-network, enhancing charge transport, redox activity, and interfacial electron transfer, thereby enabling exceptionally high SC for supercapacitor electrodes and rapid photocatalytic degradation of organic dye pollutants. By systematically validating the dual-application performance of $NiFe_2O_4$@rGO in electrochemical energy storage and environmental remediation, this work establishes a cost-effective, sustainable, and multifunctional hybrid material that bridges the gap between energy conversion and wastewater treatment.

2. MATERIALS AND METHODOLOGY

2.1 Materials

Nickel ferrite ($NiFe_2O_4$) , graphene oxide (GO) was procured from Matrics Enterprises, Nagercoil, Tamil Nadu, India. Sodium hydroxide (NaOH) was obtained from Kovai Cheenu Enterprises, Coimbatore, Tamil Nadu, India. Deionized water was utilized throughout entire process.

2.2 Synthesis of Nickel Ferrite

Nickel ferrite ($NiFe_2O_4$) nanoparticles were synthesized using a sol–gel auto-combustion method. Stoichiometric amounts of nickel nitrate hexahydrate and iron nitrate nonahydrate were dissolved in deionized water with citric acid as a fuel, maintaining a 1:2 precursor-to-fuel ratio (Srinivasan *et al.* 2025). The solution was heated at 80 °C under continuous stirring until gel formation, followed by self-combustion. The resulting powder was ground and annealed at 600 °C for 3 h to obtain the crystalline spinel phase.

2.3 Synthesis of Reduced Graphene Oxide

Graphene oxide (GO) was produced with modified Hummers' technique. Subsequently, GO was subjected to thermal reduction to yield reduced rGO by heat treatment at 280 °C for 3 hours (Srinivasan *et al.* 2025). This technique provides removal of oxygen functional groups from GO structure, restoration of sp^2 hybridization and the cleavage of sp^3 carbon bonds. The reestablishment of π-bonding among carbon atoms improves electrical conductivity. The residual oxygen content and electrical conductivity were modified by changing reduction conditions, hence influencing material's electronic and functional properties.

2.4 Preparation of $NiFe_2O_4$@rGO by Green Synthetic Approach

The $NiFe_2O_4$@rGO hybrid was synthesized *via* a green mechanochemical approach by integrating $NiFe_2O_4$ nanoparticles with reduced graphene oxide (rGO). rGO was dispersed in distilled water through ultrasonication, followed by the gradual addition of $NiFe_2O_4$ under continuous stirring to ensure uniform distribution. Ethanol was used in minimal quantity to improve dispersion and prevent agglomeration, without compromising the overall solvent-reduced mechanochemical nature of the synthesis. The resulting slurry was dried at 80 °C, gently ground, and mildly

annealed at 300 ℃ for 2 h to enhance interfacial bonding while preserving the spinel structure.

2.5 Electrochemical Evaluation

The electrochemical characteristics of $NiFe_2O_4$@rGO hybrid, pristine rGO, and pristine $NiFe_2O_4$ were evaluated in three-electrode cell correct conditions. Three-electrode cell had a mercury oxide / mercury reference electrode, an active material on nickel ,and a platinum wire counter electrode foam serving as working electrode. The working electrode was constructed with carbon black, active material, PVDF, and N-methyl-2-pyrrolidinone. The slurry was prepared and coated onto the cleaned Ni foam with geometric area of 1 × 1 cm^2 by a cosmetic brush. Coated nickel foam was kept in an oven for 10 hours at 60 ℃. Discharging (GCD) / galvanostatic charging and CV measurements was achieved within the potential window of -0.1 to +0.5 V. EIS investigations were performed with a frequency of 0.01 Hz - 100 kHz. C_s was computed by

$$C_s = \frac{I \times dt}{m \times \Delta V} \quad \ldots (1)$$

$$\eta = 100 \times \frac{td}{tc} \quad \ldots (2)$$

In this context, ΔV refers to the voltage window, m indicates the active mass, dt shows discharge time, I shows current, whilst tc and td signify charging and discharging durations,

2.6 Fabrication of Symmetric Supercapacitor

About 2 g of PVA was mixed with 10 mL of distilled water in a glass beaker and stirred until a homogeneous mixture was obtained. Subsequently, 1 g of NaOH was added, and the mixture was continuously agitated in a water bath at 80 ℃ for roughly 2 hours until the gel achieved complete clarity. The gel was kept at room temperature for cooling. Filter papers were immersed in the gel for a specified duration and subsequently placed between the electrodes of $NiFe_2O_4$@rGO hybrid. The CV and GCD were evaluated within the 0–0.5 V potential range.

2.7 Photocatalytic Test

Photocatalytic experiments were studied using rhodamine B dye (RhB) by UV irradiation. The sample was exposed to UV radiation in the upper portion of reactor. In all experiments, 10 mg of the sample was dispersed in 50 mL of RhB solution and ultrasonicated for 5 minutes to ensure a homogeneous suspension. Before UV irradiation, the synthesized catalyst suspension was subjected to magnetic agitation for 30 minutes in the dark to evaluate adsorption/desorption. Under continuous agitation and controlled conditions, the diluted solution was exposed to UV irradiation at an intensity of 122 mW/cm^2.Thereafter, the concentration of RhB was determined using Vis-NIR (visible and near-infrared) spectrometry (Shimadzu UV 2550) at a wavelength of 556 nm, employing the subsequent equation:

$$\text{Degradation } (\%) = 100 \times \frac{Co - Ct}{Co} \quad \ldots (3)$$

C_t and C_0 represent starting and final concentration of RhB. Furthermore, five cycles were analysed to evaluate stability and reusability. In summary, the same photocatalyst was employed for the initial cycle, after which it was centrifuged and washed with distilled water to remove adsorbed species. The recovered specimen was subsequently dried in an oven at 70 °C.

2.8 Trapping Species Experiment

The photodegradation ($NiFe_2O_4$, rGO, and $NiFe_2O_4$@rGO hybrid) were then analyzed using a reactive species trapping method to identify the active radicals involved. Ammonium oxalate (AO), Isopropyl alcohol (IPA) and P-benzoquinone (BQ), was analysed for O_{2-}, h_+, and OH to analyze reactive samples. The trapping experiments were conducted under identical conditions with the addition of 2 μM of the trapping agent.

2.9 Material Characterizations

The XRD patterns were acquired utilizing a Bruker D8 diffractometer with Ni-filtered CuKα to ascertain phases in the samples. The specific surface areas of the compounds were ascertained by BET method (Anton Paar Autorb iq, USA) utilizing a surface area analyzer, employing a nitrogen isotherm at −189 ℃. The specimen underwent degassing at 140 ℃ for 3 hours. The absorption spectra were acquired by JASCO V-770 UV–vis over wavelength range of 190–3200 nm at room temperature. Samples for UV–vis analysis were dissolved in deionized water to get a homogeneous suspension. The composition and morphology of materials were examined utilizing field-emission scanning electron microscopy (ZEISS, Gemini).

3. RESULTS AND DISCUSSIONS

3.1 Evaluation of Structural Behaviour

Fig. 1 depicts the crystalline properties and phase purity of produced rGO, $NiFe_2O_4$, and $NiFe_2O_4$@rGO hybrid, as analyzed using powder XRD. The XRD pattern confirms crystalline structure of $NiFe_2O_4$ and $NiFe_2O_4$@rGO (hybrid). The diffraction

peaks of pristine $NiFe_2O_4$ closely align with standard patterns. Additionally, within the two diffraction peaks of the $NiFe_2O_4$@rGO hybrid, notable diffraction peaks are ascribed to (220), (311), (400), (511), and (440) planes; a prominent diffraction peak at $2\theta = 28.96°$ was observed, corresponding to the (002) crystallographic plane of rGO.

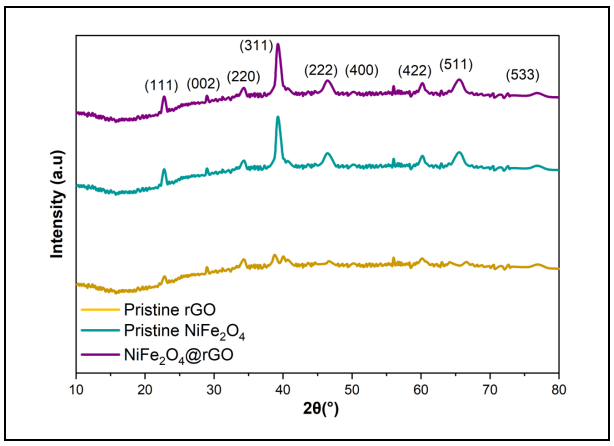


Fig. 1: XRD pattern for rGO, $NiFe_2O_4$ and $NiFe_2O_4$@rGO

BET study were performed to approve surface characteristics of $NiFe_2O_4$@rGO hybrid (Fig. 2). The porosity and specific surface area was evaluated using N_2 Barrett-Joyner-Halenda (BJH) and adsorption/desorption techniques. The unaltered rGO, unaltered $NiFe_2O_4$, and $NiFe_2O_4$@rGO hybrid desorption / adsorption. Surface areas of $NiFe_2O_4$, $NiFe_2O_4$@rGO hybrid were measured at 5.59 $m^2\ g^{-1}$, and 4.12 $m^2\ g^{-1}$. Although BET analysis shows a slight reduction in the specific surface area of the $NiFe_2O_4$@rGO hybrid, this is attributed to partial coverage of $NiFe_2O_4$ nanoparticles by rGO sheets. Importantly, the formation of a conductive nano-network enhances charge transport and redox accessibility, increasing the number of electrochemically active sites despite the reduced physical surface area. Pore volume of $NiFe_2O_4$@rGO hybrid diminished (from 0.085 $cm^3\ g^{-1}$) compared to rGO and $NiFe_2O_4$, known to raise transfer resistance of electrolyte ions.

The ultraviolet (UV) characteristics of reduced graphene oxide (rGO), nickel ferrite ($NiFe_2O_4$), and the $NiFe_2O_4$@rGO hybrid was evaluated by UV-visible spectrophotometry, as depicted in Fig. 3. Pristine rGO exhibits stronger UV absorption in the UVB region compared to $NiFe_2O_4$. However, a decrease in absorption was observed beyond 244 nm, with a distinct absorption edge at 322 nm. The UV spectra of pure $NiFe_2O_4$ display two different absorption band edges within the range 320 to 420 nm and 620 to 720 nm. The edges relate to plasma resonance absorption of $NiFe_2O_4$. The integration of rGO with $NiFe_2O_4$ significantly enhanced light absorption across the 200–800 nm wavelength range. Fig. 4 illustrates the summary of ultraviolet absorption over the different spectra zones. $NiFe_2O_4$@rGO hybrid displayed a reduced bandgap of 1. 3 eV compared to the bandgaps of rGO (about 0.8eV) and $NiFe_2O_4$ (around 1.00 eV) is shown in Fig. 5.

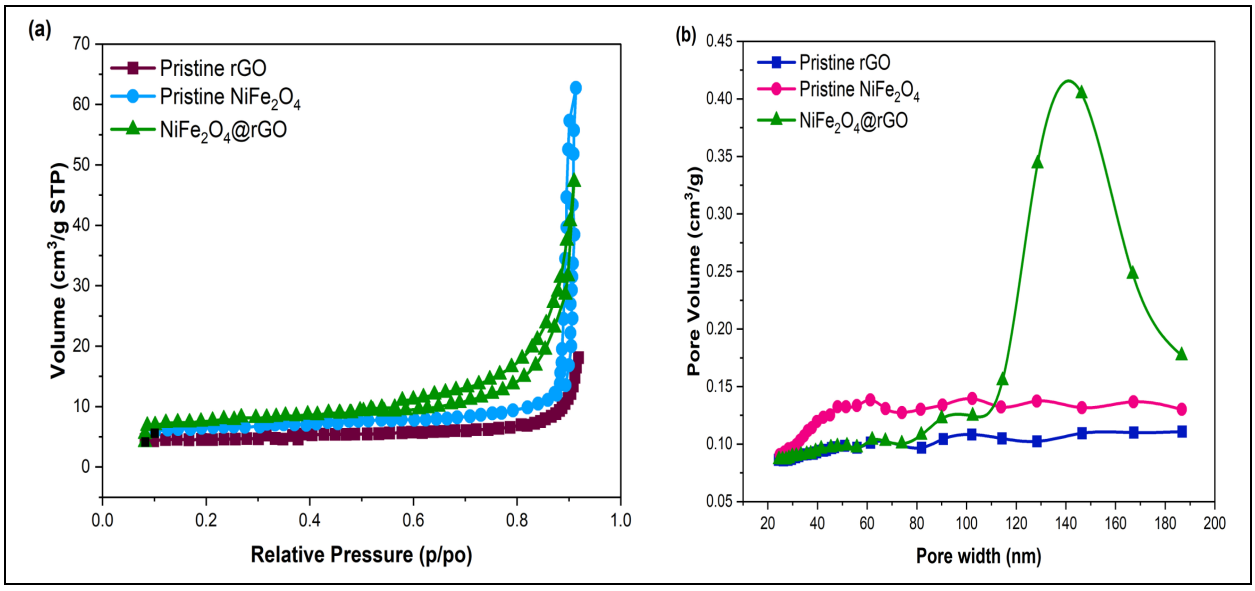


Fig. 2: Porosity analysis using N_2 isotherms and BJH curves

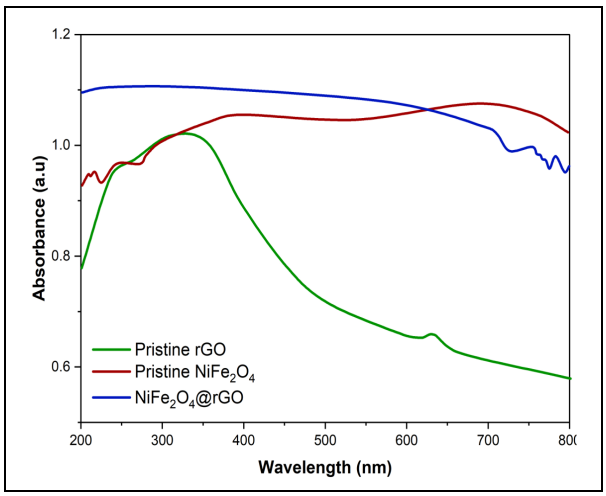


Fig. 3: UV absorption spectra of pristine rGO, pristine $NiFe_2O_4$ and $NiFe_2O_4$@rGO

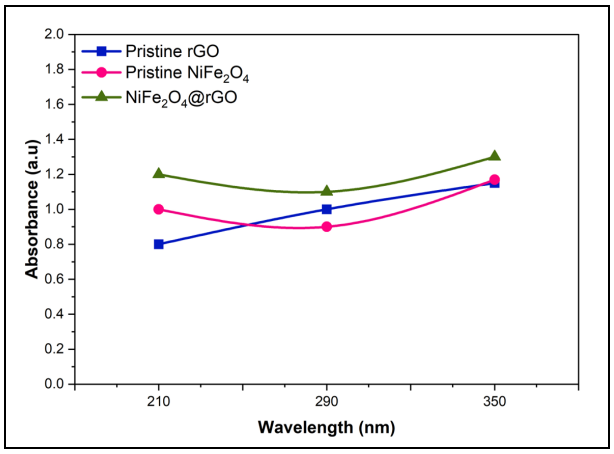


Fig. 4: Comparative UV absorption intensities at selected wavelengths

X-ray photoelectron spectroscopy (XPS) was employed to investigate the elemental composition and oxidation states of the $NiFe_2O_4$@rGO hybrid (Fig. 6). The survey spectra confirm the presence of Ni, Fe, C, and O, with no extraneous elements detected, indicating successful hybrid formation. The Ni 2p spectrum exhibits two main peaks at approximately 855.6 eV (Ni $2p_{3/2}$) and 873.3 eV (Ni $2p_{1/2}$), along with characteristic satellite peaks, confirming the presence of Ni^{2+} species in the spinel $NiFe_2O_4$ structure. The Fe 2p spectrum shows distinct peaks at around 711.0 eV (Fe $2p_{3/2}$) and 724.5 eV (Fe $2p_{1/2}$), corresponding to Fe^{3+} oxidation state. The O 1s spectrum can be deconvoluted into multiple components, with peaks centered at ~529.6 eV attributed to lattice oxygen (metal–oxygen bonds in $NiFe_2O_4$), ~530.8 eV associated with oxygen vacancies or defect-related oxygen, and ~531.8 eV corresponding to surface-adsorbed oxygen or hydroxyl groups. The C 1s spectrum confirms the presence of rGO, showing contributions from sp^2-hybridized C–C bonds and residual oxygen-containing functional groups. These results collectively confirm the successful formation of the $NiFe_2O_4$@rGO hybrid and strong interfacial interaction between $NiFe_2O_4$ nanoparticles and rGO sheets.

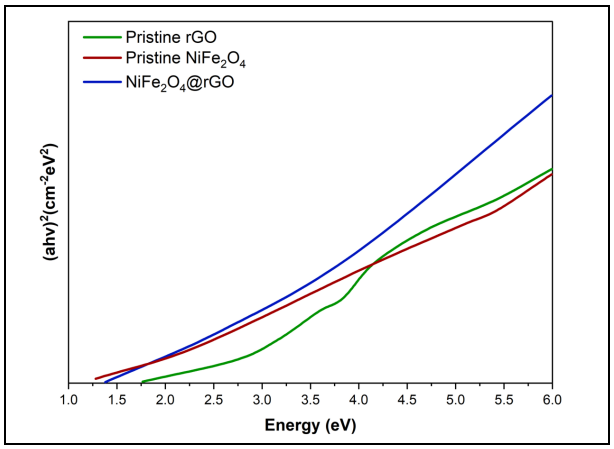


Fig. 5: Tauc's plot for $NiFe_2O_4$ and $NiFe_2O_4$@rGO hybrid

Fig. 7 depicts the morphology of rGO, $NiFe_2O_4$, and $NiFe_2O_4$@rGO porous spheres, showcasing the nanoporous architecture. The pristine rGO has a sheet-like morphology but SEM pictures of pure $NiFe_2O_4$ show agglomerated particles. Fig. 7 distinctly demonstrates that the hybrid $NiFe_2O_4$@rGO was produced with a sponge-like porous interconnecting architecture.

3.2. Electrochemical analysis

The electrochemical efficiency of $NiFe_2O_4$@rGO hybrid was evaluated by galvanostatic charge-discharge profiles and cyclic voltammetry, measured at −0.1 to +0.5 V at 4.0 M NaOH (Girimurugan *et al.* 2024). Fig. 8 illustrates the comparative cyclic voltammetry profiles of pristine reduced graphene oxide (rGO), pristine nickel ferrite ($NiFe_2O_4$), and $NiFe_2O_4$@rGO hybrid electrodes at scan rate of 3.8 mV/s.

The non-rectangular CV profile shows that charge storage primarily arises from the pseudo-capacitance mechanism, resulting from the reversible redox process. The prominent redox peaks were chiefly ascribed to Faradaic reaction at $NiFe_2O_4$.

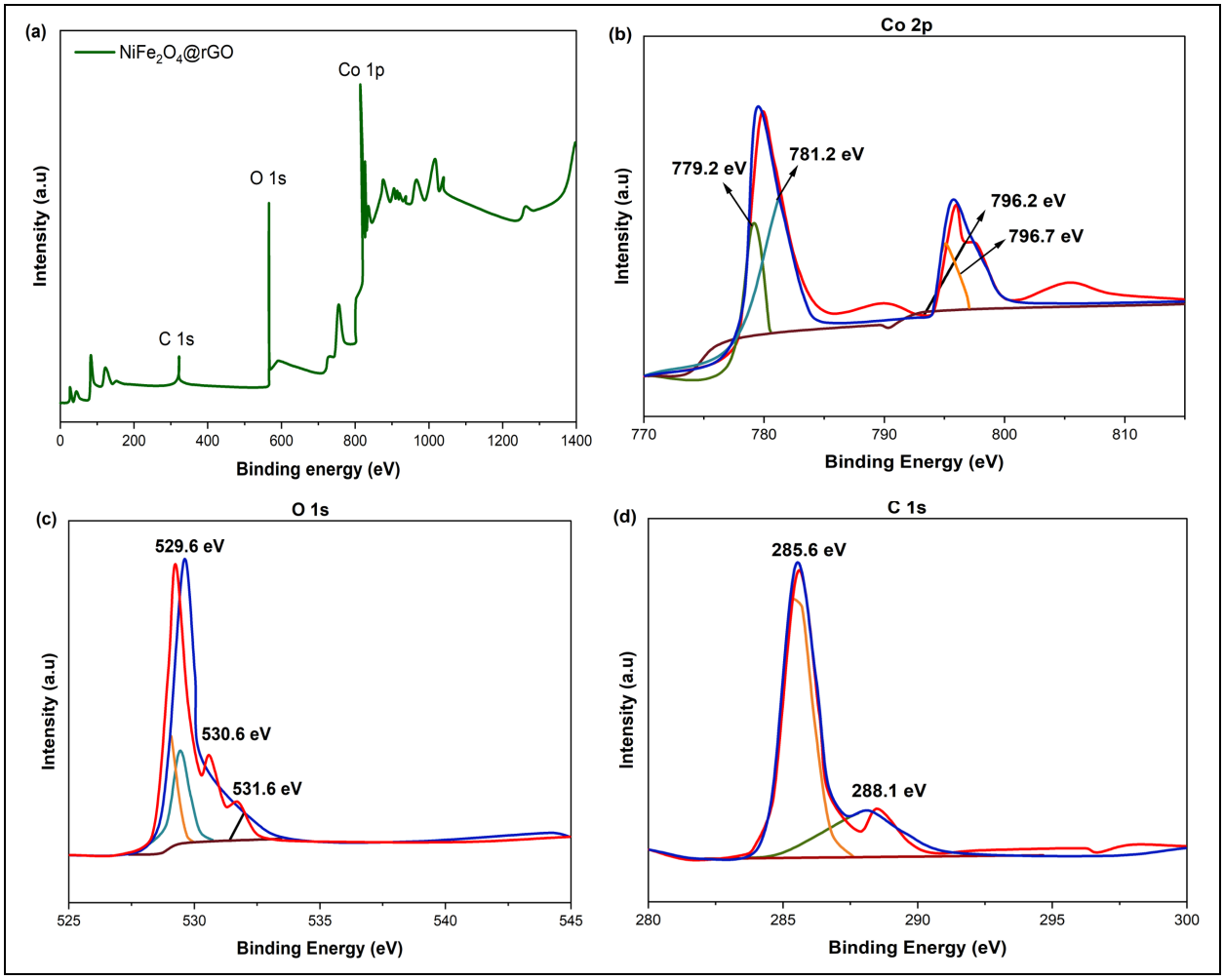


Fig. 6: XPS analysis of $NiFe_2O_4$@rGO: survey and elemental spectra

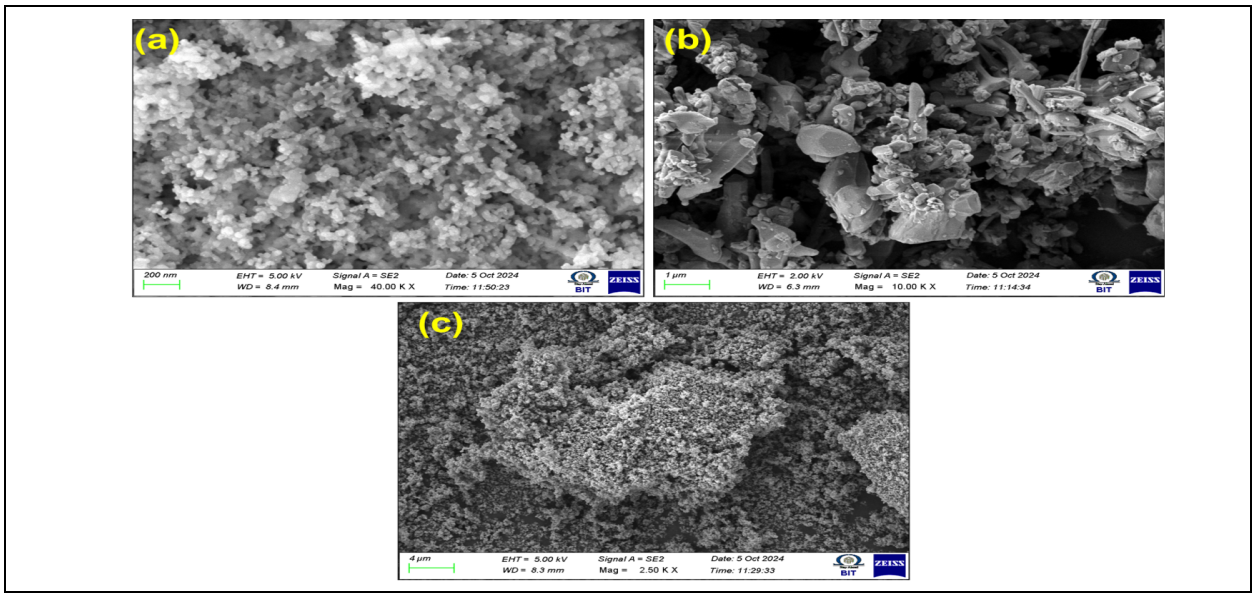


Fig. 7: SEM images (a) rGO, (b) $NiFe_2O_4$, (c) $NiFe_2O_4$@rGO

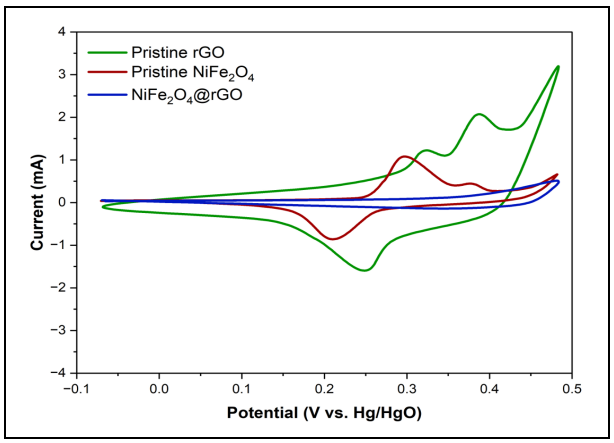


Fig. 8: Cyclic voltammetry of rGO, $NiFe_2O_4$, and hybrid electrodes;

$$CoOOH + OH^- \leftrightarrow CoO_2 + H_2O + e^- \quad \ldots (4)$$

$$Co_3O_4 + OH + H_2O \leftrightarrow 3CoOOH + e^- \ldots (5)$$

CV of $NiFe_2O_4$@rGO hybrid electrode displays redox peaks. Nonetheless, a displacement at reduction and oxidation peak was noted, ascribed to significant C_3N_4 on $NiFe_2O_4$ during redox reaction. Pristine rGO exhibits typical electric double-layer capacitive behavior, characterized by quasi-rectangular CV profiles and short discharge durations, indicating rapid surface charge adsorption but limited charge storage capacity. $NiFe_2O_4$ shows distinct redox peaks associated with reversible Faradaic reactions, confirming pseudocapacitive behavior. However, its electrochemical performance is constrained by poor electrical conductivity and higher charge-transfer resistance. The $NiFe_2O_4$@rGO hybrid combines the advantages of both components, exhibiting enhanced redox current response, prolonged discharge times, and reduced internal resistance. The rGO network facilitates efficient electron transport, while $NiFe_2O_4$ provides abundant redox-active sites, resulting in superior electrochemical performance. The voltammograms maintained their structure at an increased scan rate of 50 mVs^{-1}, its results were mentioned in Fig. 9. The CV profile of $NiFe_2O_4$@rGO hybrid electrode mostly maintained its shape despite the presence of redox peaks, signifying improved reversibility during rapid discharging and charging cycles.

An improved high-rate discharge capability is crucial for assessing electrode materials at supercapacitor efficiency. $NiFe_2O_4$@rGO hybrid, rGO, and $NiFe_2O_4$ electrodes were subjected to discharging and charging profiles at current density of 1 A g^{-1} of −0.1 to +0.5 V; outcomes are shown in Fig. 10. Double-layer capacitor, nonlinear discharge curve demonstrates pseudo-capacitance of $NiFe_2O_4$. The outcomes demonstrate that $NiFe_2O_4$@rGO hybrid electrode possesses longest discharge time in comparison to rGO and $NiFe_2O_4$ electrodes, hence showing superior capacitance. Fig. 11 depicts the GCD profile of the $NiFe_2O_4$@rGO hybrid electrode at current density of 1, 2, 3, and 5 A g−1. GCD profiles of unaltered $NiFe_2O_4$ and unaltered rGO electrodes at densities of 1, 2, 3, and 5 A g^{-1}. C_s values calculated by Equ. (1) were 496, 345, 275, and 119 F $g^{-1}Fg^{-1}$, for the $NiFe_2O_4$@rGO hybrid electrode; 119.83, 206, 28 and 118 Fg^{-1}, for $NiFe_2O_4$; and 65, 39, 14 and 24 Fg^{-1}, for rGO on 1, 2, 3, and 5 Ag^{-1} (Fig. 12). The $NiFe_2O_4$@rGO hybrid electrode maintains a high capacitance of 83.28 Fg^{-1} at 5 Ag^{-1}.

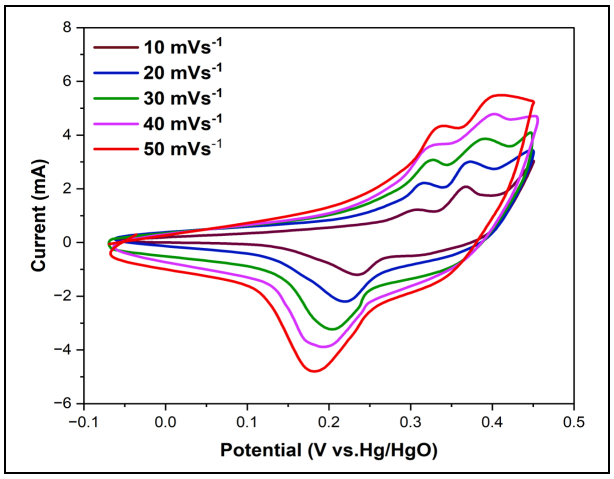


Fig. 9: Properties of three electrode measurement: (b) CV profiles 10–50 $mV.s^{-1}$ for $NiFe_2O_4$@rGO hybrid electrode

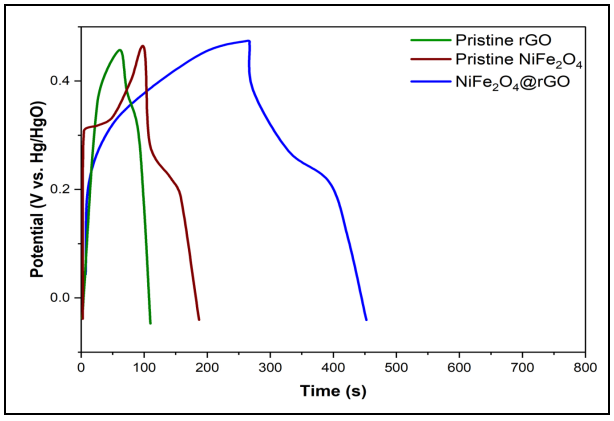


Fig. 10: GCD comparison of rGO, $NiFe_2O_4$, and $NiFe_2O_4$@rGO electrodes

Fig. 13 illustrates Nyquist plot representing fitting data, with the component Z″ plotted against the real component Z for rGO, $NiFe_2O_4$, and $NiFe_2O_4$@rGO hybrid electrodes. Rs of $NiFe_2O_4$@rGO electrode (1.3 Ω) were significantly lower pure $NiFe_2O_4$ (1.7 Ω) and rGO (2 Ω). Findings demonstrate that $NiFe_2O_4$@rGO hybrid electrode possesses enhanced conductivity compared to the unmodified $NiFe_2O_4$ electrode. As reported in earlier studies, ternary $NiFe_2O_4$/rGO/PPy nanocomposite provided five-fold raise in capacitance compared to $NiFe_2O_4$ due to improved conductivity and electron

transport. The asymmetric supercapacitor achieved an energy density of 29.2 Wh kg^{-1} with good cycling (Kasif *et al.* 2025). Charge transfer resistance (R_{ct}) of $NiFe_2O_4$@rGO hybrid electrode recorded at 1.17 Ω, markedly lower than $NiFe_2O_4$ electrode (1.46 Ω) and rGO (2.29 Ω), shows an enhanced charge transfer rate at $NiFe_2O_4$@rGO hybrid electrode with GCD the and CV profiles.

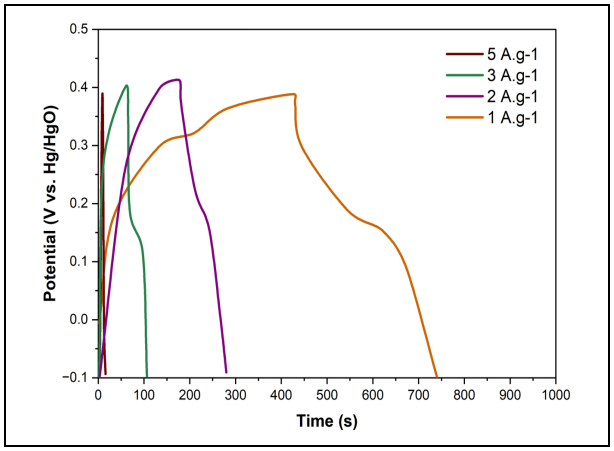


Fig. 11: Rate-dependent GCD profiles of $NiFe_2O_4$@rGO hybrid electrode

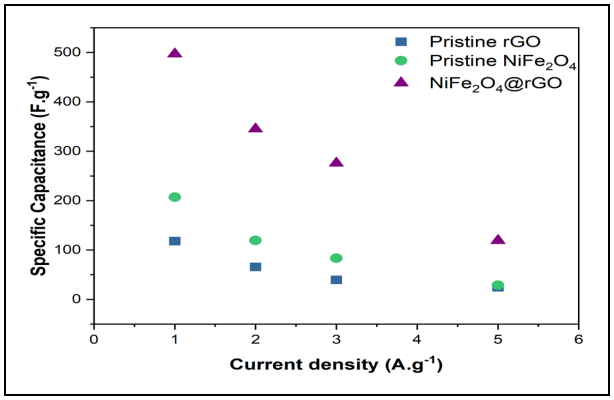


Fig. 12: Specific capacitance variation with current density for different electrodes

As summarized in Table 1, the $NiFe_2O_4$@rGO hybrid prepared *via* a green mechanochemical route delivers competitive capacitance and excellent cycling stability compared to recently reported $NiFe_2O_4$–rGO systems synthesized using more complex or solvent-intensive methods.

A supercapacitor was created by two electrodes to demonstrate the possible applicability of the improved $NiFe_2O_4$@rGO hybrid. Fig. 14 depicts the cyclic voltammetry profiles of $NiFe_2O_4$@rGO at different scan rates across 0–0.5 V potential range. The shape of CV profile was ascribed to charge storage mechanism. As a result, CV profiles have quasi-rectangular shape lacking identifiable peaks, signifying superior capacitive efficiency. Moreover, CV profiles maintained their integrity at high scan rates demonstrating rapid discharging and charging capacities.

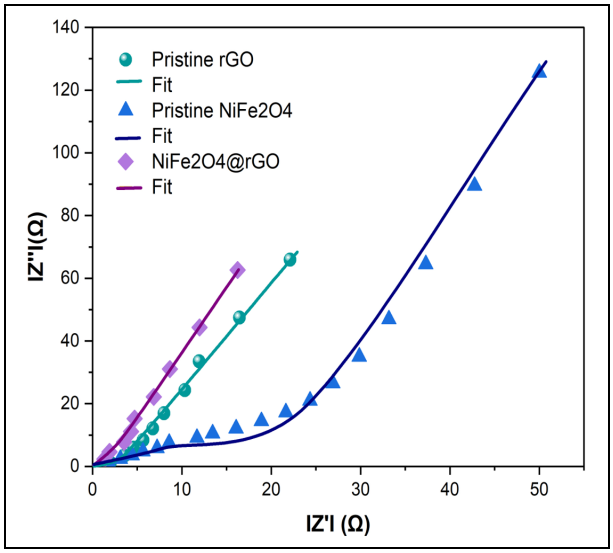


Fig. 13: Properties three electrode measurements: for EIS measurement rGO, $NiFe_2O_4$ and $NiFe_2O_4$@rGO hybrid electrode

3.3 Symmetric Supercapacitor Evaluation

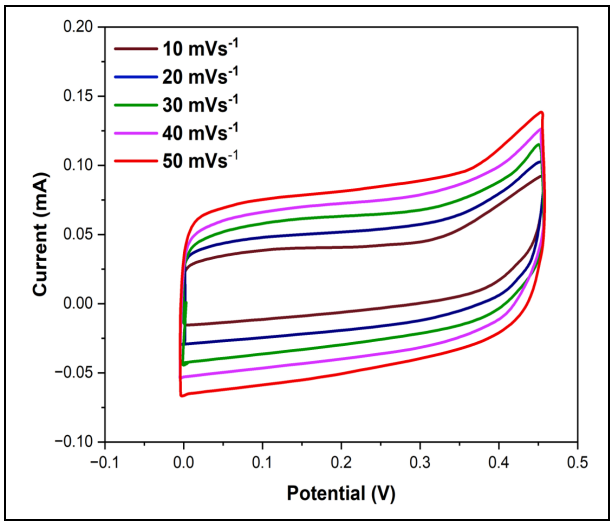


Fig. 14: Scan-rate-dependent cyclic voltammetry of $NiFe_2O_4$@rGO hybrid

To analyze the stability efficiency of the device, many CV cycles was analyzed at 0.3 V, depicted in Fig. 15. Enhanced $NiFe_2O_4$@rGO hybrid device showed remarkable stability with increased rates exerting no influence on its electrochemical performance, hence signifying greater rate capability.

Triangular topologies of discharging/charging profiles at different densities validate enhanced electrochemical characteristics of optimized $NiFe_2O_4$@rGO hybrid device, as depicted in Fig. 16.

Table 1. Comparative electrochemical performance of $NiFe_2O_4$–rGO based electrodes

Material system	Synthesis Method	Electrolyte	Specific Capacitance (F g^{-1})	Cycling Stability	Reference
$NiFe_2O_4$/rGO fiber	Sol–gel + electrospinning	KOH	650 at 1 A g^{-1}	92% (5000 cycles)	(Gad *et al.* 2026)
Yb–$NiFe_2O_4$/rGO	Waste-derived chemical route	KOH	926 at 1 A g^{-1}	90% (5000 cycles)	(Vinoth *et al.* 2025)
Co-doped $NiFe_2O_4$/rGO/MWCNT	Sol–gel	KOH	295.8 at 1 A g^{-1}	85.5% (5000 cycles)	(Vijayakanth *et al.* 2025)
$Cu_{0.5}Ni_{0.5}Fe_2O_4$–rGO–TiO_2	Hydrothermal	NaOH	410 at 1 A g^{-1}	88% (4000 cycles)	(Sadiq *et al.* 2025)
$NiFe_2O_4$/rGO	Microwave-assisted	KOH	1320 C g^{-1}	94% (5000 cycles)	(Carmel *et al.* 2022)
$NiFe_2O_4$@rGO (this work)	Green mechanochemical one-pot	4 M NaOH	496 at 1 A g^{-1}	93.16% (5000 cycles)	Present study

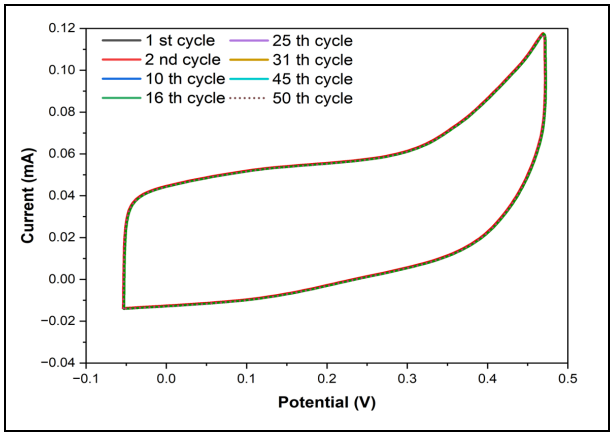


Fig. 15: Electrochemical performance of symmetric solid-state $NiFe_2O_4$@rGO supercapacitor

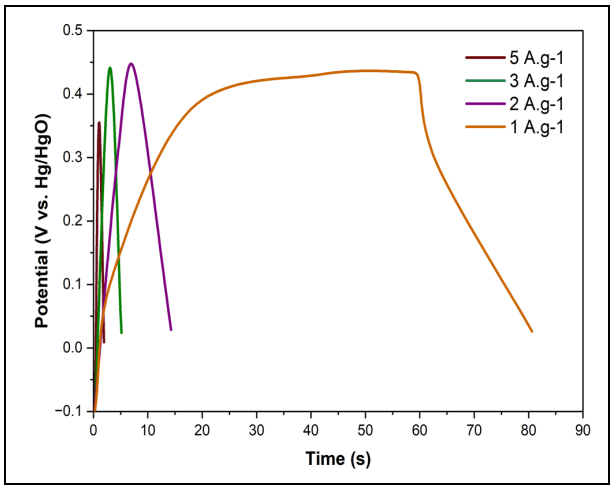


Fig. 16: GCD profiles of symmetric $NiFe_2O_4$@rGO supercapacitor at varying currents

The enhanced $NiFe_2O_4$@rGO hybrid symmetric device, exhibiting current density of 1.0 Ag^{-1}, has superior SC (about 103 Fg^{-1}). The C_s values were roughly 31.07 Fg^{-1}, 46.94 Fg^{-1}, and 47.17 Fg^{-1} as illustrated in Fig. 17.

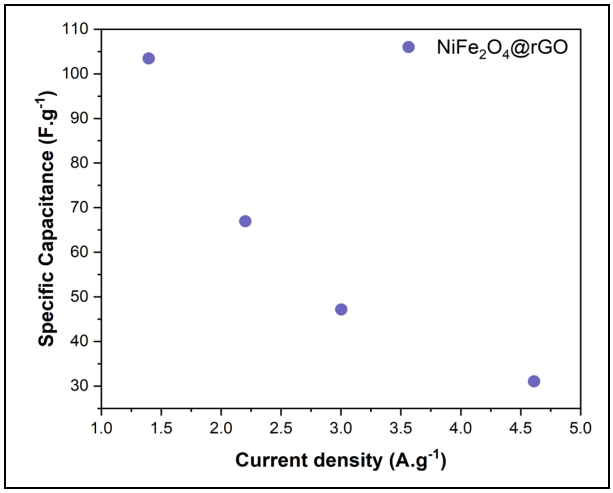


Fig. 17: Specific capacitance variation in $NiFe_2O_4$@rGO with current density

The cycle performance employing the GCD profile is a vital measure in practical uses. Cycling lifespan of optimized $NiFe_2O_4$@rGO hybrid device was assessed at a current density 10 A g^{-1} throughout potential of 0 V to 0.5 V. According to earlier studies, KCu_7S_4/rGO nanocomposites grown *in situ* on flexible stainless-steel mesh exhibited an ultrahigh C_S of 1747.4 F g^{-1} at 1 A g^{-1}. The assembled flexible symmetric supercapacitor delivered 60.4 Wh kg^{-1} with 72% retention after 6000 cycles (Mo *et al.* 2026). The outcomes depicted in Fig. 18 were remarkably advantageous. The device retained around 93.16% capacitance after 5000 charge-discharge cycles.

EIS further confirmed the feasibility of electronic transport at enhanced $NiFe_2O_4$@rGO hybrid device. Fig. 19 presents Nyquist curve of optimized $NiFe_2O_4$@rGO hybrid device, with the inset illustrating corresponding circuit. The R_{ct} and R_s values were recorded at roughly 0.345 Ω and 0.765 Ω, confirming the improved conductivity, signifying low resistance of this device. The findings confirm enhanced $NiFe_2O_4$@rGO

hybrid demonstrates considerable potential owing to the exceptional capacitive efficiency of the device.

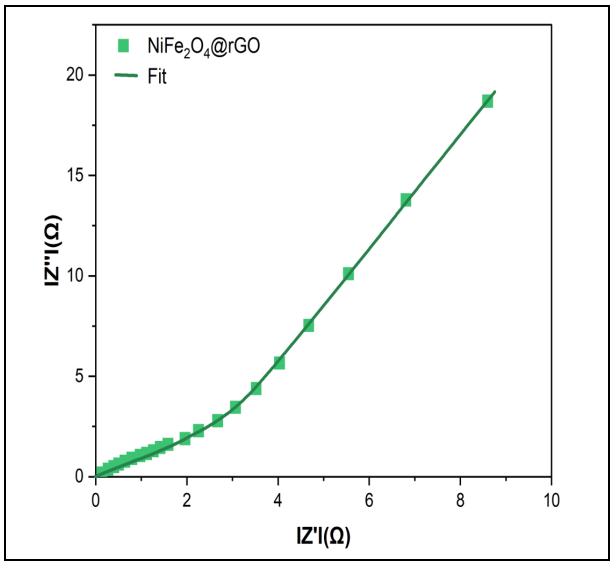


Fig. 18: EIS spectra of pristine and $NiFe_2O_4$@rGO symmetric supercapacitors

3.3 Equivalent Circuit Fitting Analysis

To quantitatively validate the EIS interpretation (Table 2), the impedance spectra were fitted using an equivalent circuit model consisting of solution resistance (R_s), charge-transfer resistance (R_{ct}), constant phase element (CPE), and Warburg diffusion element (W). The fitted parameters confirm the improved conductivity and faster charge-transfer kinetics of the $NiFe_2O_4$@rGO hybrid compared to pristine electrodes.

Coulombic performance is an essential criterion for evaluating electrode stability of devices in practical applications. The coulombic efficiency of $NiFe_2O_4$@rGO hybrid device was analyzed at a current density of 10 A g^{-1} at 5000 cycles. The coulombic performance was assessed utilizing Equ (2). It approached 92% during 1000 cycles, with a 4.5% decline in capacitance noted after 3000 cycles. The device retained 93.16% of its initial capacitance after 5000 cycles with a density of 10 Ag^{-1}. This cycling performance is due to remarkable stability resulting from enhanced electronic conductivity. At a current density of 5 A g^{-1}, the electrode exhibited a Coulombic efficiency of 93.16% over 5000 charge–discharge cycles. Results demonstrate that $NiFe_2O_4$@rGO symmetric device shows diminished coulombic performance at low densities, which enhances at high current densities owing to its superior capability. The maximum energy density and power density were 12.2 Wh kg^{-1} and 1322 W kg^{-1}, respectively. In prior studies, rGO–Co_3O_4 nanocomposites exhibited excellent electrochemical performance, achieving a high C_S of 1006 F g^{-1} in a symmetric supercapacitor device. The device showed 80% stability over 10,000 cycles with 100% coulombic efficiency, supporting portable energy storage applications (Babu *et al.* 2026). The remarkable capacitive efficiency of $NiFe_2O_4$@rGO hybrid device can be attributed to its carefully engineered morphology, which offers an expanded surface area.

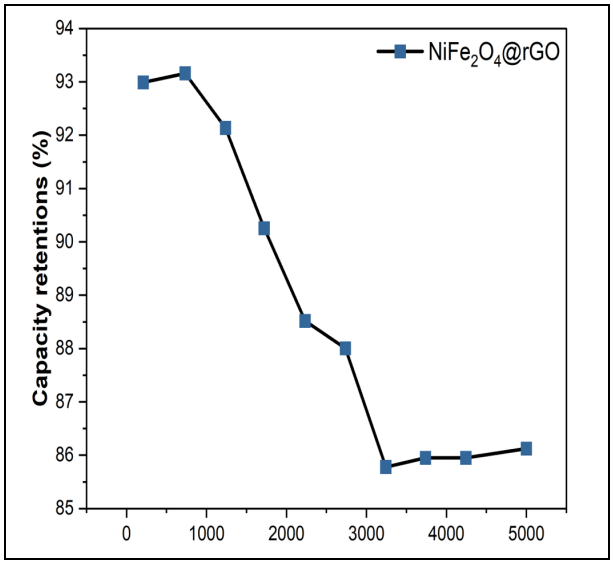


Fig. 19: Cycling stability and capacitance retention at 10 A g^{-1}

Table 2. Equivalent circuit fitting parameters obtained from EIS analysis

Electrode	Rs (Ω)	Rct (Ω)	CPE ($F \cdot s^{n-1}$)	n	W ($\Omega \cdot s^{-1/2}$)
rGO	2.00	2.29	0.0016	0.82	1.15
$NiFe_2O_4$	1.70	1.46	0.0023	0.85	0.92
$NiFe_2O_4$@rGO hybrid	1.30	1.17	0.0041	0.89	0.61

3.4 Evaluation of Photocatalytic Activity

Fig. 20-23 demonstrates effectiveness of RhB photodegradation when subjected to UV irradiation. The RhB exhibited a peak absorption maximum at 528 nm (S8). A control experiment using RhB was performed to confirm that photolysis was suppressed, as the absorption spectra exhibited only a minimal decrease after 60 minutes of UV irradiation (Muruganandhan *et al.* 2023). In low-light conditions, the absorption intensity of RhB remained constant in the presence of the $NiFe_2O_4$@rGO hybrid, signifying no desorption or adsorption. The RhB absorption spectra displayed negligible deterioration when mixed with pristine $NiFe_2O_4$ in darkness. After approximately 60 minutes of UV irradiation, RhB experienced gradual degradation attributed to the existence of pristine $NiFe_2O_4$, as depicted in the absorption spectra (Fig. 20).

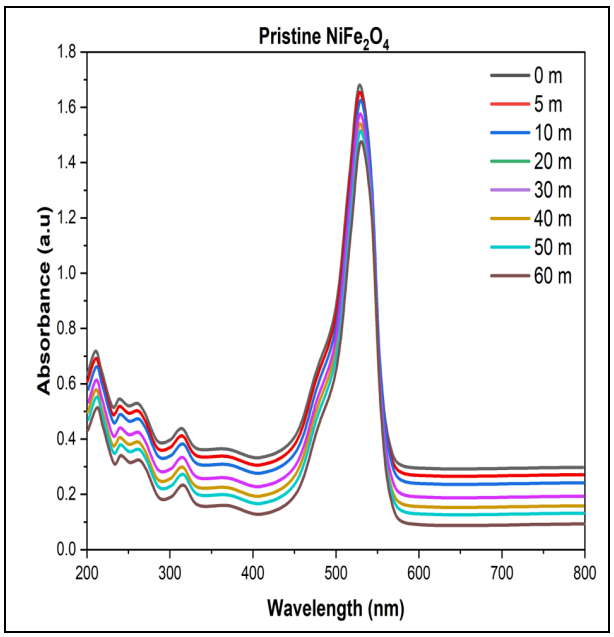


Fig. 20: UV-driven photocatalytic activity of $NiFe_2O_4$@rGO hybrid

The incorporation of rGO markedly improved the degradation efficiency of RhB, highlighting its synergistic interaction with $NiFe_2O_4$ under UV irradiation. The results are illustrated in Fig. 21. About 52% of RhB was degraded during first 20 minutes and almost completely removed after 50 minutes of UV irradiation. Findings show that $NiFe_2O_4$@rGO hybrid exhibited superior photocatalytic performance compared to pure $NiFe_2O_4$, presumably attributable to chemical and morphological characteristics of produced structure. The rGO-integrated $NiFe_2O_4$ exhibits remarkable photocatalytic due to synergistic effect, suggesting that $NiFe_2O_4$@rGO hybrid is a promising candidate for effective photocatalytic applications.

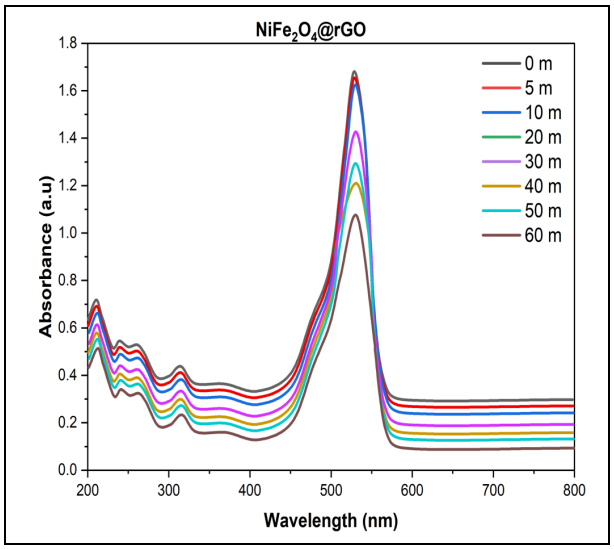


Fig. 21: UV-driven photocatalytic performance of $NiFe_2O_4$

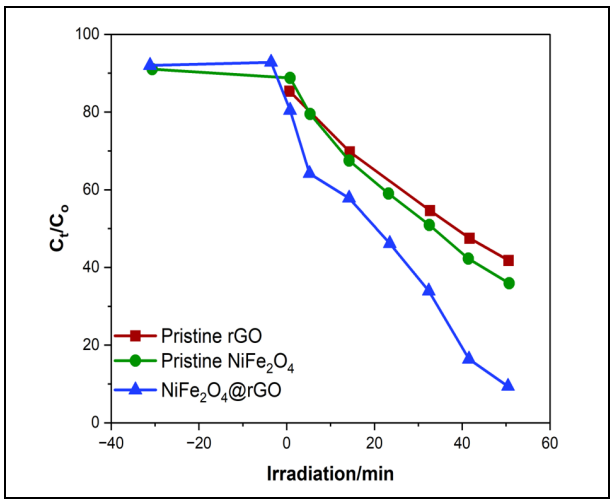


Fig. 22: C_t/C_0 variation with UV irradiation time

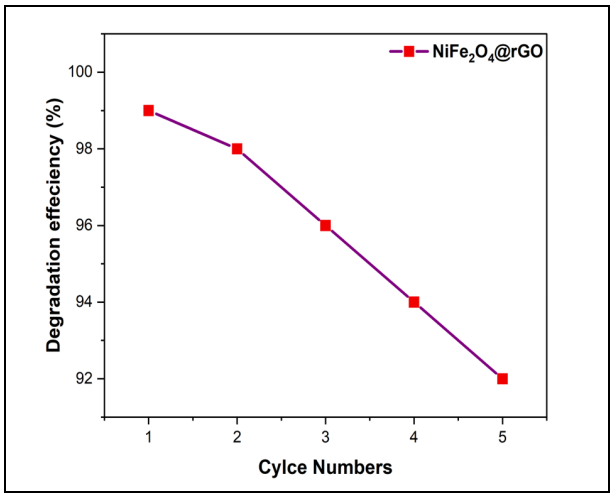


Fig. 23: Photocatalytic stability: degradation efficiency versus cycle number

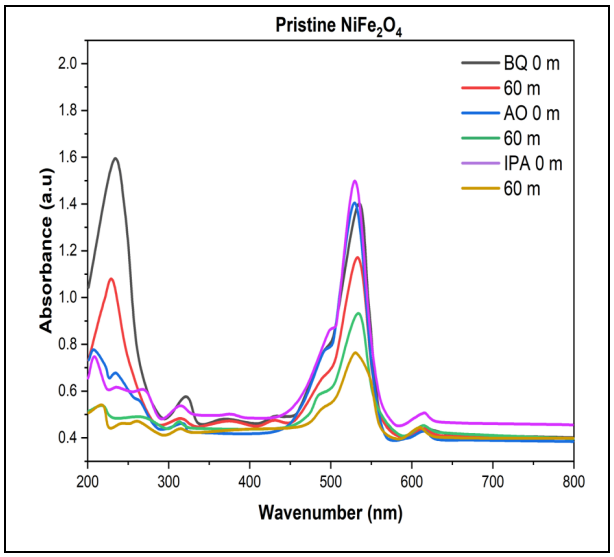


Fig. 24: Active species trapping study of pristine $NiFe_2O_4$ under UV

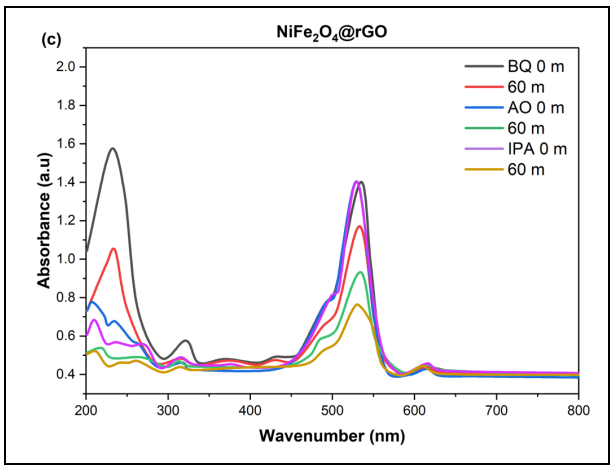


Fig. 25: Active species trapping study of pristine rGO under UV

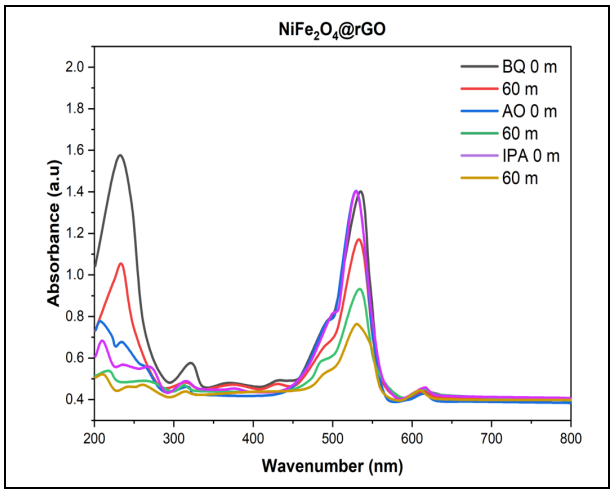


Fig. 26: Active species trapping study of $NiFe_2O_4$@rGO under UV

The reusability and stability of the $NiFe_2O_4$@rGO hybrid photocatalyst were evaluated for the degradation of RhB dye during five successive cycles under UV irradiation. Fig. 23 demonstrates that the photocatalytic efficiency of the $NiFe_2O_4$@rGO hybrid for degrading RhB dye remained stable after 5 cycles, showing approximately 99% lower at degradation efficiency, suggesting that $NiFe_2O_4$@rGO hybrid can serve as a reliable catalyst for photodegradation.

3.5 Evaluation of Active Trapping

The photocatalytic reaction employing $NiFe_2O_4$, rGO, and $NiFe_2O_4$@rGO hybrids, investigations involving the entrapment of reactive species were performed utilizing trapping agents. Figure 24-27 illustrates absorption RhB in the presence and absence of radical scavengers, employing $NiFe_2O_4$, rGO, and $NiFe_2O_4$@rGO hybrids. The RhB degradation exceeded those of pure $NiFe_2O_4$ on the inclusion of IPA (OH) when compared to AO (h^+) and BQ (O^{-2}), as depicted in Fig. 24. RhB with rGO in the presence of radical scavengers was similarly recorded (Fig. 25). The incorporation of IPA into RhB solution with $NiFe_2O_4$@rGO hybrid led to a reduction of almost 50% in the RhB relative to those produced with pure rGO and pure $NiFe_2O_4$. Earlier findings reported that, the biowaste-derived rGO decorated with NiO and $NiFe_2O_4$ nanoparticles exhibited excellent multifunctionality. The composite also showed high visible-light photocatalytic efficiency of 96.5%, indicating dual energy–environmental applications (Tamilselvi *et al.* 2022).

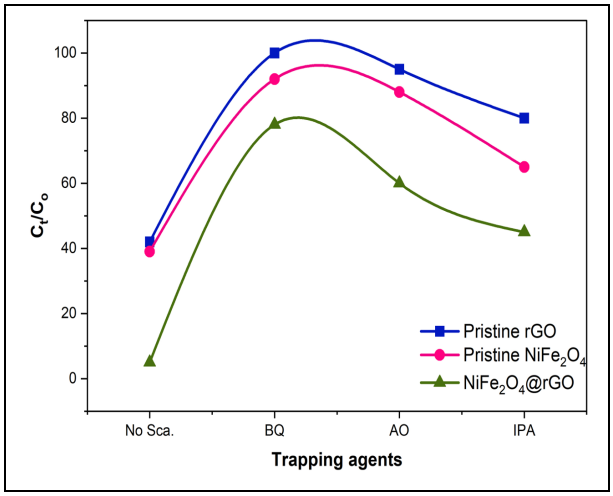


Fig. 27: Effect of scavengers on C_t/C_0 during UV photocatalysis

4. CONCLUSION

A $NiFe_2O_4$@rGO hybrid was successfully synthesized *via* a green mechanochemical one-pot approach, offering a sustainable and scalable route for multifunctional material development. Structural and surface analyses (XRD, XPS, SEM, BET, and UV–Vis) confirmed the successful formation of the hybrid with strong interfacial coupling between $NiFe_2O_4$ nanoparticles and rGO sheets. Although the BET surface area showed a slight reduction after hybridization, the formation of a conductive rGO network significantly enhanced charge transport and redox accessibility, leading to improved electrochemical performance. The $NiFe_2O_4$@rGO hybrid delivered a high specific capacitance of 496 F g^{-1} at 1 A g^{-1} in a three-electrode configuration and exhibited good rate capability and cycling stability. The assembled symmetric supercapacitor retained 93.16% of its initial capacitance after 5000 cycles, demonstrating reliable long-term performance. In addition, the hybrid showed excellent photocatalytic activity, achieving over 99% degradation of rhodamine B under UV irradiation, with $\bullet O_2^-$ identified as the dominant reactive species. The enhanced electrochemical and photocatalytic performances arise from the synergistic interaction between $NiFe_2O_4$ and rGO rather than surface area effects alone. This study

highlights the potential of mechanochemically synthesized $NiFe_2O_4$@rGO hybrids as promising candidates for sustainable energy storage devices and environmental remediation applications, while offering a pathway for future development of multifunctional, eco-friendly materials.

FUNDING

This research received no specific grant from any funding agency in the public, commercial, or not-for-profit sectors.

CONFLICTS OF INTEREST

The authors declare that there is no conflict of interest.

COPYRIGHT

This article is an open-access article distributed under the terms and conditions of the Creative Commons Attribution (CC BY) license (http://creativecommons.org/licenses/by/4.0/).



REFERENCES

Alburaih, H. A., Ahtisha, M., Atiq, U. R., Batool, Z., Hassan, R. U., Musa, S. H. E. M. and Noor, N. A., Synergistic effect of conducting polymer PANI on electrochemical performance of Ni ferrites for asymmetric supercapacitors, *J. Inorg. Organomet, Polym. Mater.,* 35(10), 8613–8626 (2025). https://doi.org/10.1007/s10904-025-03595-w

Anantha, R. L., Satishkumar, P., Nagabhooshanam, N., Rao, P. K. V., Kumar, D. S., Chakravarthy, A. K., Prasad, Y. D. and Mohanavel, V., Shear strength, wear, thermal conductivity, and hydrophobicity behavior of fox millet husk biosilica and Amaranthus dubius stem fiber–reinforced epoxy composite: a concept of biomass conversion, *Biomass Convers. Biorefin*., 15(2), 2893–2901 (2025). https://doi.org/10.1007/s13399-023-04854-x

Babu, C. R., Anila, E. I. and Avani, A. V., Aqueous symmetric supercapacitor based on hydrothermally grown reduced graphene oxide wrapped cobalt oxide nanocomposites, *Fuel,* 406, 137225 (2026). https://doi.org/10.1016/j.fuel.2025.137225

Carmel, J. M. B., Judith, V. J., Saravanakumar, B., Bououdina, M. and John, K. L. J., $NiFe_2O_4$ and 2D-rGO decorated with $NiFe_2O_4$ nanoparticles as highly efficient electrodes for supercapacitors, *Synth. Met*., 291, 117201 (2022). https://doi.org/10.1016/j.synthmet.2022.117201

Chu, D., Li, F., Song, X., Ma, H., Tan, L., Pang, H., Wang, X., Guo, D. and Xiao, B., A novel dual-tasking hollow cube $NiFe_2O_4$–NiCo-LDH@rGO hierarchical material for high-performance supercapacitor and glucose sensor, *J. Colloid Interface Sci*., 568, 130–138 (2020). https://doi.org/10.1016/j.jcis.2020.02.012

Gad, S., Rafea, M. A., Elfawal, G. E., Zaki, M. E. A., Elsharkawy, S. G. and Khalil, H. F., Temperature dependent crystallinity, DFT calculations and electrochemical behavior of $NiFe_2O_4$/reduced graphene oxide fiber electrodes for high-performance supercapacitors, *Mater. Res. Bull*., 195, 113845 (2026). https://doi.org/10.1016/j.materresbull.2025.113845

Girimurugan, R., Selvaraju, M., Shine, S. and Khaled, J. M., Investigation on polypyrrole-induced modification of Aspergillus flavus: evaluation of biocompatibility and electrochemical properties, *J. New Mater. Electrochem. Syst.,* 27(3), 190–198 (2024). https://doi.org/10.14447/jnmes.v27i3.a04

Hiragond, A. S., Shinde, B. T., Narale, D. K. and Chavan, H. V., Hydrothermally synthesized nickel ferrite microstructures for supercapacitor, *Solid State Commun.,* 406, 116183 (2025). https://doi.org/10.1016/j.ssc.2025.116183

Hsu, T. E., Krishtappa, M., Ho, M. K., Chiu, H. H., Yu, S. L., Lyu, B. L., Yu, Y. T., Kuo, H. C., Yu, S. W., Cheng, C. L., Shidaling, M., Hanumanthappa, N., Chen, M. C., Huang, Y. L. and Wu, S. Y., High-performance Bi-doped $NiFe_2O_4$ nanoparticles for advanced supercapacitors and room-temperature magnetic memory applications, *ACS Appl. Electron. Mater*., 7(9), 3704–3724 (2025). https://doi.org/10.1021/acsaelm.5c00021

Jiang, L., Mei, X., Gan, D., Song, S., Lei, X., Cai, F., Wang, Y., Zhang, Q., Lu, X. and Ren, Z., Hybrid transition-metal oxide and nitride@N-doped reduced graphene oxide electrodes for high-performance flexible all-solid-state supercapacitors, *Chem. Eur. J.,* 27(18), 5761–5768 (2021). https://doi.org/10.1002/chem.202005096

Kandavalli, S. R., Prabhu, S. V., Devi, K. V., Raja, P. G. N., Kasi, U. K., Rajesh, S., Rajesh, K. B., Selvaraju, M., Shine, K. and Jamal, K. M., Bioresin-based hybrid green composite preparation using Holoptelea integrifolia fibers reinforced by Ziziphus jujuba seed particles: a fuzzy logic assisted optimization of mechanical behaviour, *Z. Phys. Chem*., 239(5), 747–772 (2025). https://doi.org/10.1515/zpch-2024-0837

Kasif, M., Zimik, M., Hussain, S., Devi, M. and Thangavel, R., High-performance hybrid supercapacitor using $NiFe_2O_4$/rGO/polypyrrole ternary composite derived from Prussian blue analogs, *J. Am. Ceram. Soc.,* 108(12) (2025). https://doi.org/10.1111/jace.70181

Khawale, V. R., Mayank, Kumar, R., Satishkumar, P., Barun, H., Deepa, B., Saminathan, R., Veeramanikandan, P., Babu, P. A. S. and Mayakannan, S., Study on electrochemical stability and charge transfer efficiency for the development of high-performance supercapacitors using iron oxide (Fe_2O_3) nanorods, *J. New Mater. Electrochem. Syst*., 27(3), 163–171 (2024). https://doi.org/10.14447/jnmes.v27i3.a01

Manohar, A., Suvarna, T., Vattikuti, S. V. P., Sudhani, H. P. K., Manivasagan, P., Jang, E. S., Ali, B. A., Naresh, M. and Kim, K. H., Ternary nanocomposites of $ZnFe_2O_4$/$NiFe_2O_4$/CeO_2: investigating electrochemical energy storage and biocompatible properties, *J. Environ. Chem. Eng*., 12(5), 113337 (2024). https://doi.org/10.1016/j.jece.2024.113337

Mo, Y., Zhang, K.,Wu, F., Xian, H., Shi, X., Li, W., Chen, S. and Qin, A., In-situ growth and electrodeposition of KCu_7S_4/rGO on flexible mesh for high-energy-density supercapacitors, *Electrochim. Acta*, 546, 147808 (2026). https://doi.org/10.1016/j.electacta.2025.147808

Moradi, S. A. H. and Ghobadi, N., Fabrication of composite GO/$NiFe_2O_4$–$MnFe_2O_4$–$CoFe_2O_4$ anode material: toward high-performance hybrid supercapacitors, *Microsc. Res. Tech*., 87(10), 2459–2474 (2024). https://doi.org/10.1002/jemt.24615

Muruganandhan, P., Jothilakshmi, S., Vivek, R., Nanthakumar, S., Sakthi, S., Mayakannan, S. and Girimurugan, R., Investigation on silane modification and interfacial UV aging of flax fibre reinforced with polystyrene composite, *Mater. Today Proc*., (2023). https://doi.org/10.1016/j.matpr.2023.03.272

Razzaq, K., Haifa, A. A., Alrowaily, A. W., Alobati, B. M., Eman, A., Kumar, A. and Hassan, R. U., Improved electrochemical performance of $MgCr_2O_4$/rGO nanohybrid for supercapacitor applications, *J. Phys. Chem. Solids*, 210, 113331 (2026). https://doi.org/10.1016/j.jpcs.2025.113331

Sadiq, M., Singh, A. K., Vidhi, and Thakur, O. P., Fabrication and electrochemical insights into advanced rGO-modified ternary Cu-doped $NiFe_2O_4$/TiO_2 electrodes for high-performance supercapacitors, *Ceram. Int*., 51(5), 5679–5694 (2025). https://doi.org/10.1016/j.ceramint.2024.12.016

Saha, S., Routray, K. L. and Parida, A., Graphene-integrated Ag-doped $NiFe_2O_4$ nanostructures for high-performance supercapacitor application, *Diam. Relat. Mater.,* 155, 112264 (2025). https://doi.org/10.1016/j.diamond.2025.112264

Sahoo, B. B., Thatoi, D. N., Pandey, V. S. and Nayak, M. K., Microsphere-like $MnFe_2O_4$/rGO/SnS_2 nanocomposite material for supercapacitor electrode, *Mater. Lett.,* 405, 139782 (2026). https://doi.org/10.1016/j.matlet.2025.139782

Sardana, S., Kanika, A., Malik, S., Saini, A., Dahiya, S., Dahiya, S., Punia, R., Maan, A. S., Singh, K. and Ohlan, A., Unveiling the surface-dominated capacitive properties in flexible ternary polyaniline/$NiFe_2O_4$/reduced graphene oxide nanocomposite hydrogel electrode for supercapacitor applications, *Electrochim. Acta*, 434, 141324 (2022). https://doi.org/10.1016/j.electacta.2022.141324

Srinivasan, S. A., Mekala, R., Rajadesingu, S. and Monisha, P., Tunable properties of Ce^{3+}-doped nickel ferrite: insights into cation redistribution, bandgap modulation and magnetic behaviour, *Ceram. Int*., 51(25), 44326–44339 (2025). https://doi.org/10.1016/j.ceramint.2025.07.163

Tamilselvi, R., Lekshmi, G. S., Padmanathan, N., Selvaraj, V., Bazaka, O., Levchenko, I., Bazaka, K. and Mandhakini, M., $NiFe_2O_4$/rGO nanocomposites produced by soft bubble assembly for energy storage and environmental remediation, *Renew. Energy*, 181, 1386–1401 (2022). https://doi.org/10.1016/j.renene.2021.07.088

Utami, M., Amalia, R. M., Indra, P., Gani, P., Yenn, T. W., Husniati, Sadaf, S., Taisan, A. N., Nouraf, A. F., Amani, A. M., Badar, A. A. Alam, M. W., Green biogenic synthesis of Ag-loaded TiO_2/rGO nanocomposite and its prospective applications in antibacterial and self-cleaning surface coating, *Mater. Chem. Phys.,* 348, 131573 (2026). https://doi.org/10.1016/j.matchemphys.2025.131573

Veeramani, T., Venkataraju, C., Ramesh, G., Dinesh, A., Lalitha, G., Patil, R. P., Ayyar, M., Influence of ZnO on structural magneto-optical dielectric and antibacterial properties of ZnO–$NiFe_2O_4$ nanocomposites prepared by sol–gel method, *Inorg. Chem. Commun*., 171, 113615 (2025). https://doi.org/10.1016/j.inoche.2024.113615

Vijayakanth, V., Kummara, M. R., Vijayababu, M., Krishnamoorthi, K., Al-Zahrani, F. A. M. and Rosaiah, P., Synergistic effects in Co-doped $NiFe_2O_4$/rGO/MWCNT ternary nanocomposites for enhanced supercapacitor performance, *Diam. Relat. Mater*., 158, 112679 (2025). https://doi.org/10.1016/j.diamond.2025.112679

Vinoth, S. K., Alhamzani, A. G., Mortaga, A. K. M., Ehab, A. A., Saad, A. A., Arun, V., Raghu, M. S. and Kumar, K. Y., Upcycling waste plastics into rGO–Yb@$NiFe_2O_4$ hybrid electrodes for high-performance supercapacitors and hydrogen evolution, *Diam. Relat. Mater.,* 159, 112898 (2025). https://doi.org/10.1016/j.diamond.2025.112898